Biomimetic, stiff and adhesive periosteum with osteogenic-angiogenic coupling effect for bone regeneration

Yuhe Yang, Tianpeng Xu, Qiang Zhang, Yun Piao, Ho Pan Bei, Xin Zhao*

Y. Yang., T. Xu., Q. Zhang., Y. Piao, H. P. Bei., Dr. X. Zhao.
Department of Biomedical Engineering, The Hong Kong Polytechnic University, Hung Hom, Hong Kong, China
Email: xin.zhao@polyu.edu.hk

Abstract: Current periosteal grafts have limitations related to low mechanical strength, tissue adhesiveness, and poor osteogenesis and angiogenesis potential. Here, we develop a periosteum mimicking bone aid (PMBA) with similar structure and function to natural periosteum by electrospinning photo-crosslinkable methacrylated gelatin (GelMA), L-arginine-based unsaturated poly (ester amide) (Arg-UPEA), and methacrylated hydroxyapatite nanoparticles (nHAMA). Such combination of materials enhances the material mechanical strength, favors the tissue adhesion, and guarantees the sustained activation of NO-cGMP signaling pathway, with well-coordinated osteogenic-angiogenic coupling effect for accelerated bone regeneration. This work presents a proof-of-concept demonstration of thoroughly considering the progression of implant biomaterials: that is, the initial material components (i.e., GelMA, Arg-UPEA and nHAMA) equip the scaffold with suitable structure and function, while its degradation products (i.e., Ca^{2+} and L-arginine) are involved in long-term mediation of physiological activities. We envision our strategy will inspire the design of high-performance bioscaffolds towards bone and periosteum tissue engineering.

1. Introduction

Periosteum is a fibrous connective tissue membrane that encases the outer surface of most bones.[1] Due to its high osteogenic and angiogenic capability, periosteum has been widely recognized for its remarkable regenerative capacity and is believed to play a decisive role in both physiological bone formation and pathological defect reconstruction.[2] A working

periosteum is essential to both prevention of bone nonunion and treatment of severe fractures, especially for osteoporotic and diabetic patients with impaired stability and blood supply at the fracture site.[3] Currently artificial periostea for bone defect repair applications are usually made of cell sheets,[4] porcine small intestinal submucosa,[5] acellular dermis,[6] hydrogels,[7] and electrospun membranes.[8] Among them, electrospun membranes are promising as they resemble the fibrous nature of periosteum and have a high surface area to volume ratio, high porosity as well as suitable physical strength.[7, 9] In more recent years, composite electrospun membranes like Polycaprolactone (PCL)/gelatin,[10] Poly (l-lactic acid) (PLLA)/hydroxyapatite,[11] and PLLA/strontium borosilicate glasses[12] have been put forward to remedy polymers' hydrophobic nature, slow biodegradation and lack of bioactive moieties; however, these scaffolds have low tissue adhesion property, which fail to adhere to the defect site. Most importantly, most of these studies focused only on the osteogenic activity of the artificial periosteum and overlooked its angiogenesis capability;[8] as well as an oversight to the complicated interplay between each added components of their artificial periostea and the underlying molecular mechanism during bone/periostea regeneration, rendering their designs too complicated for practical feasibility.

Here, we develop a periosteum mimicking bone aid (PMBA) with similar structure to natural periosteum, appropriate mechanical strength and flexibility for easy handling, excellent tissue adhesion property to allow material-bone fixation and integration, and synergistic co-osteogenesis and -angiogenesis capability for better bone healing. We fabricate the PMBA by electrospinning a mixture of methacrylated gelatin (GelMA), L-arginine-based unsaturated poly (ester amide) (Arg-UPEA) and methacrylated hydroxyapatite nanoparticles (nHAMA) (Figure 1). Upon light exposure, these three components crosslink with each other to form an organic-inorganic co-crosslinked double network. GelMA is used due to its biocompatibility and tissue adhesiveness thanks to the presence of multiple domains to bind to the cell surface receptors and extracellular matrix protein.[7, 9, 13] nHAMA is incorporated to improve the

mechanical performances of our PMBA and as a calcium ion (Ca^{2+}) reservoir. Cationic Arg-UPEA is added to further increase the adhesion strength of PMBA by electrostatic attractions and covalent binding with carboxyl groups of bone tissue surface.[14] It also works as the precursor to provide adequate L-arginine for subsequent nitric oxide (NO) production[14a, 15] by NO synthase (NOS) in presence of Ca^{2+} (released from nHAMA).[13c, 16] NO is an endogenous signaling molecule that plays a critical role in bone repair by simultaneously stimulating the angiogenic and osteogenic cascades.[17] The continuous supply of L-arginine and Ca^{2+} from PMBA, along with sufficient NO production are found to trigger soluble guanylate cyclase (sGC) leading to the upregulation of downstream signaling molecules like cyclic guanosine monophosphate (cGMP) and protein kinase (PKG), which in turn ensures the sustained activation of NO/cGMP signaling pathway and subsequently achieves a well-coordinated osteogenic-angiogenic coupling effect during bone repair. To the best of our knowledge, this is the first study to date that incorporates the molecular mechanism of both osteogenesis and angiogenesis into the design of biomimetic periosteum and provide a proof-of-concept demonstration of orchestrating the progression of implant biomaterials: that is, the initial material components (i.e., GelMA, Arg-UPEA and nHAMA) equip the scaffold with suitable physical and biological properties, while its degradation products (i.e., Ca^{2+} and L-arginine) are also involved in long-term mediation of physiological activities, effectively achieving the biomaterials trio: replacement, enhancement, and assimilation. We envision that our PMBA will have great clinical potential to substitute the natural periosteum for prevention of bone nonunion, and in case of severe fractures, hastened recovery in combination with bone grafts.

2. Results and discussion

2.1. Characteristics of synthesized GelMA, Arg-UPEA and nHAMA

To prepare PMBA, we first synthesized GelMA by chemical modification of gelatin with methacrylic anhydride, as confirmed by the distinctive double peak at around 5.5 ppm (peak 1

and 2) in the [1]H-nuclear magnetic resonance (^{1}H NMR) spectrum (Figure. S1A). Arg-UPEA was obtained following our previous protocol,[18] and its chemical structure was verified by ^{1}H NMR and Fourier transform infrared (FTIR) spectroscopy (Figure. S1B and C). nHAMA of ~100 nm diameter was synthesized by grafting hydroxyethyl methacrylate (HEMA) to the surface of nanohydroxyapatite (nHA) via hexamethylene diisocyanate (HDI) (Figure. S1D). FTIR spectroscopy and thermogravimetric analysis (TGA) further validated the successful conjugation of HDI-HEMA chain to HA (Figure. S1E and F). As expected, these HDI-HEMA brushes not only improved the colloidal stability of nHAMA in ethanol, but also endowed the nHAMA with photo-reactivity as evidenced by increased precipitation formation in nHAMA solution after UV radiation (Figure. S2A). A major challenge of utilizing nanoparticles in electrospinning is their inevitable aggregation due to the interparticle electrostatic interactions, which may cause blockage of needle tip.[19] To examine the feasibility of using nHAMA-containing solution in electrospinning, we further tested the colloidal stability of nHAMA in the GelMA/hexafluoroisopropanol solution. Compared with the nHA group, little precipitation formed in nHAMA-containing electrospun solutions after placement for 4 or 8 h, indicating that a more stable electrospinning process without nozzle clogging could be achieved using nHAMA-containing solution (Figure. S2B). Such difference in colloidal stability between nHA and nHAMA was possibly due to the formation of a shell shield (HDI-HEMA brushes) onto nHAMA surface, which prevented interparticle electrostatic interaction.[20] However, with the increase of nHAMA content, we observed an obvious stratification and precipitation formation in the 20%nHAMA group (Figure. S2B), and thus the solid contents of nHAMA at 5% and 10% were adopted to prepare the electrospinning solutions in the following studies.

2.2. Morphology, water sorption, water retention and degradation of PMBA

We prepared PMBA by first electrospinning a mixed precursor containing different contents of the GelMA, Arg-UPEA and nHAMA, and then exposing the electrospun membranes to UV

light to form a stable co-crosslinked organic-inorganic double network. To fully explore the effects of Arg-UPEA and nHAMA on physiochemical and biological performances of PMBA, a total of seven groups of electrospun membranes were prepared including G (pristine GelMA), G/5HM (GelMA/5%nHAMA), G/10H (GelMA/10%nHA), G/10HM (GelMA/10%nHAMA), G/1A/10HM (GelMA/1%Arg-UPEA/10%nHAMA), G/5A/10HM (GelMA/5%Arg-UPEA/10%nHAMA), G/10A/10HM (GelMA/10%Arg-UPEA/10%nHAMA).

The surface morphology of PMBA was observed via scanning electron microscopy (SEM), which showed a uniform, smooth and randomly oriented nanofibrous structure with no significant difference in the fiber diameter (Figure. 2A and B). The average fiber diameter was found in the range of 242.6 ± 58.3 to 267.8 ± 62.5 nm. This nanofibrous structure mimics the structure of natural periosteum which is vital to the function of the resident cells.[8, 21] Transmission electron microscopy (TEM) further revealed an even distribution of nHAMA in the fiber without significant agglomeration (Figure. S3). These results demonstrated that the addition of nHAMA and Arg-UPEA to GelMA precursor does not bring significant changes to the fiber diameter, enabling production of an extracellular matrix (ECM)-mimicking nanofibrous scaffold.

Next, we evaluated the *in vitro* water uptake and degradation of PMBA as they have huge implications for drug/molecule release and practical applications.[22] Our results showed that PMBA membranes exhibited distinct water sorption after immersing in phosphate buffer saline (PBS) (absorbed at least 8-9 times the amount of water of their dry weight), and such water sorption was highly dependent on the incorporated Arg-UPEA contents but not on nHAMA or nHA contents (Figure. S4A). This phenomenon was further attested by the SEM images of post-swelling PMBA in which the fiber diameter increased to ~800 nm (Fig. 2A and B). In addition, we found that GelMA/Arg-UPEA/nHAMA showed significantly prolonged water retention as compared to GelMA, GelMA/nHA or GelMA/nHAMA (9-10 days vs 3-4 days) after being removed from water (Figure. S4B). The favorable water sorption and holding

capacity of PMBA could be explained partly by (1) formation of a looser network structure with lower crosslinking density resulted from Arg-UPEA, and (2) presence of many hydrophilic groups like ester and amide bonds in Arg-UPEA. These unique characteristics bestowed upon PMBA good ability to transport nutrients and wastes, and mediate cell recruitment, exudate absorption and ECM deposition during bone reconstruction. Next, *in vitro* degradation test showed that all hydrogel membranes exhibited obvious mass losses (i.e. degradation behavior) with different degradation rate after 28 days' incubation (Figure. S4C). Increasing the nHAMA content decreased the degradation rate, which was likely due to the formation of higher crosslinking-density network in the system. However, a slightly hastened degradation was observed with increasing Arg-UPEA content in PMBA, which could be attributed to higher water sorption and faster degradation of Arg-UPEA component.[23] These results proved that the degradation performance of PMBA can be finely turned using different GelMA/Arg-UPEA/nHAMA ratios to suit subsequent *in vivo* applications.

2.3. Mechanical and adhesive strength of PMBA

To maintain structural integrity during implantation while avoiding unnecessary damage of surrounding tissues, artificial periostea should possess rigorous mechanical properties. Thus, we examined the mechanical properties of PMBA by tensile stress-strain measurements. Our results demonstrated that the mechanical performances of PMBA could be enhanced by increasing the nHAMA content (Figure. 2C and D). Compared with G/10H, G/10HM possessed higher tensile modulus and fracture strain, probably owing to the improved interfacial bonding between the nHAMA and GelMA as well as an even distribution of nanofiller in the polymer matrix. In addition, we found that there are no significant changes in the mechanical properties of engineered periostea despite addition of Arg-UPEA content up to 10% (w/w), with a tensile modulus of $858.35 \pm 46.29 - 946.86 \pm 74.67$ kPa, and an extensibility of $130.6 \pm 15.4 - 151.1 \pm 19.8$ % (Figure. 2C and D). Notably, such elastic modulus was comparable to the elastic

6

modulus of natural periosteum (920–1930 kPa).[24] These results showed that our PMBA exhibited remarkable mechanical tunability and could resist external forces without graft failure.

Tissue adhesiveness is another important factor for artificial periostea since they need to rapidly and stably stick to the defect site, acting as a physical barrier to prevent the ingrowth of surrounding soft tissue and withstand the pressure from both tissues and fluids, while simultaneously working as a niche to facilitate the cell recruitment for accelerated bone healing. In this experiment, we measured the burst pressure to evaluate the resistance of PMBA to blood or tissue pressure. We found that the PMBA showed a strong adhesion to the natural bone tissue once being deployed on the bone surface, with its' burst pressure improved up to 165.6 ± 8.9 mmHg by increasing Arg-UPEA content (Figure. 2E and F). Notably, the burst pressure of G/5A/10HM and G/10A/10HM were significantly higher than normal systolic pressure (<120 mmHg), indicating our PMBA could avoid detachment caused by blood flow during surgery. We further performed lap shear tests to assess the anti-detachment properties of PMBA. The results confirmed its robust adhesion performance, with adhesive strengths of all Arg-UPEA presenting groups (520 ± 51) outperforming the GelMA group (98 ± 19) and the clinically established tissue patches such as Fibrin Glue (15.4 ± 2.8 kPa) (Fig. 2G).[25]

2.4. *In vitro* cell viability, adhesion, proliferation and migration

With our PMBA's mechanical properties established, we then moved on with biocompatibility assessments. We measured the survival, adhesion, proliferation and migration of rat bone marrow stromal cells (rBMSCs) and human umbilical vein endothelial cells (HUVECs) seeded onto the scaffold surface as these cell behaviors are highly relevant to scaffold-bone integration and sequent defect repair. Our results showed that all hydrogel membrane scaffolds could support the survival (>90% cell viability), adhesion, proliferation and migration of both cell types (Figure 3, Figure. S5). Specifically, both cells exhibited obvious pseudopodia shape with evident vinculin expression indicating cell-matrix adhesion on the surface of our PMBAs, and

could form spreading monolayers after 3 days of culture (Figure 3). Quantitative analysis indicated that cell spreading area, vinculin expression, proliferation and migration increased with increasing Arg-UPEA and nHAMA concentration (Figure 3D,H, Figure S6). Electrospun hydrogel membranes with highest Arg-UPEA content exhibited maximum cell spreading area, cell vinculin numner, proliferation and migration among all the groups. The above results have collectively demonstrated our PMBA is promising for providing beneficial microenvironment for bone healing

2.5. *In vitro* osteogenesis and angiogenesis

L-arginine is known as a common precursor of NO, while Ca^{2+} has been demonstrated as an important regulator of NOS activity of NOS.[26] It is expected that the nHAMA inside PMBA can decompose and release Ca^{2+} to activate the NOS in rBMSCs and HUVECs, promoting NO generation by catalytical decomposition of L-arginine from Arg-UPEA (Figure. 4A). The elevated NO expression will further trigger downstream cascades to synergistically improve osteo- and angiogenesis during bone healing. In this regard, we first characterized the release kinetics of L-arginine and Ca^{2+} from the PMBA membranes. We found that all groups could sustainably release L-arginine and Ca^{2+} for over 30 days without any burst release, and the L-arginine and Ca^{2+} release rates were highly dependent on the initial contents of Arg-UPEA and nHAMA incorporated in the scaffolds (Figure. 4B and C).

We then investigated whether the continuous and adequate supply of L-arginine and Ca^{2+} can synergistically facilitate the NO production and activate the downstream signaling pathway. First, we measured the NOS expression of rBMSCs and HUVECs cultured on different PMBA hydrogel membranes. After 7 days of culture, the cells on the hydrogels (G/5HM, G/10H and G/10HM) with Ca^{2+} release exhibited higher NOS expression compared to naked GelMA hydrogel (Figure. 4D and E). Moreover, such Ca^{2+}-induced enhancement of NOS expression was dose-dependent since hydrogels (G/10H and G/10HM) with higher Ca^{2+}

release significantly elevated NOS level. Our results also demonstrated that there was no significant difference in NOS level among groups with same nHAMA (10%) but different Arg-UPEA contents, indicating that the NOS expression and activity in rBMSCs and HUVECs was solely tuned by Ca^{2+} (Figure. S7).

We further measured the amount of NO production by rBMSCs or HUVECs, and found that the cells on the hydrogel membranes containing higher contents of nHAMA generated more NO, which corresponded with the NOS expression change described above (Figure. S8A). This finding suggested that the Ca^{2+} released from the membranes could promote NO generation by activating the NOS. Meanwhile, a significantly increased NO production by both cell types was observed in the Arg-UPEA presenting groups (Figure. 4F). The Arg-UPEA-enhanced NO production was also dose-dependent. The expressions of downstream signaling molecules like cGMP, sGC, and PKG also followed a similar rising trend when increasing nHAMA and/or Arg-UPEA contents (Figure. 4G-K, Figure. S8B-F). Altogether, these results verified our hypothesis that L-arginine and Ca^{2+} released from PMBA can work together to activate the NO/cGMP pathway.

As the NO/cGMP pathway is coupled with osteogenesis and angiogenesis,[27] we further examined the effects of our PMBA on osteogenesis and angiogenesis *in vitro*. As shown in Figure. 5A and D, the staining and activity of alkaline phosphatase (ALP), an early marker for osteoblastic metabolic activity,[28] were significantly elevated with increasing nHAMA content after 3 and 7 days of culture. The addition of Arg-UPEA further enhanced the ALP activity of rBMSCs, with G/10A/10HM exhibiting the highest ALP expression. A similar trend was seen by the alizarin red staining (ARS),[29] an indicator of calcium mineral deposition associated with later stage osteogenesis (Figure. 5B and E). Both the nHAMA and Arg-UPEA in PMBA exerted a positive effect on matrix mineralization, and their influences were amplified with increasing contents. These findings were further confirmed by the amplified expression levels of osteogenic marker genes like collagen type I (Col-1) and osteocalcin (OCN). The Col-1 and

9

OCN expressions in G/10A/10HM groups were nearly 17.41 and 20.48 times higher than that of GelMA control group respectively (Figure. 5F and G).

The formation of a tube-like structure by endothelial cells is a critical process in angiogenesis for regeneration of functional blood vessels.[7] Hence, we performed the tube formation assay to assess the effect of our PMBA on *in vitro* endothelial tube formation of HUVECs. As shown in Figure. 5C, more distinct and vascular-like network structures were induced in GelMA with nHAMA and/or Arg-UPEA after 12-h incubation. Consistently, the quantified level of tube formation also demonstrated that the tube length and the number of branching points were significantly higher in GelMA with higher content of nHAMA and Arg-UPEA. In particular, the G/10A/10HM group (with maximum nHAMA and Arg-UPEA content) had the longest tube length of 31.2 ± 3.9 mm and the most branching points of 58.3 ± 6.6 (Figure. 5H and I), suggesting its superior capability to promote vascularization. Furthermore, angiogenesis-related gene expression of cluster of differentiation 31 (CD31) and vascular endothelial growth factor A (VEGF-A) was found showing a similar trend (Figure. 5J and K). Together, these findings reinforced the statement that the addition of nHAMA and Arg-UPEA in PMBA could effectively coordinate the early onset of osteogenic and angiogenic process via activation of the NO/cGMP pathway, which endowed the scaffolds with similar biofunctions of natural periosteum.

2.6. *In vivo* bone regeneration therapeutic efficacy

To further examine the therapeutic efficacy of our PMBA on bone regeneration, rat critical-sized calvarial defect model was used due to its excellent reproducibility, high throughput and balanced economic cost for the assessment of both osteogeneis and angiogensis potential of the membrane-like biomaterials (Figure. 6B).[7-8, 30] At 4 and 8 weeks post-operation, bone healing effect was analyzed by micro-computed tomography (micro-CT). Newly formed bone tissues inside the defect area were observed in all groups, although the amount and quality varied

greatly among these four groups (Figure. 6A). The maximum amount of dense calcified tissue was observed in the G/10A/10HM group and its bone mineral density (BMD) and bone tissue volume/total tissue volume (BV/TV) values were substantially higher compared to control groups (Blank, G and G/10HM, $p<0.05$), indicating the synergistic effect of nHAMA and Arg-UPEA on promoting osteogenesis (Figure. 6C and D). The microscopic detail in the defect area was also analyzed histologically using hematoxylin and eosin (H&E) and Masson's trichrome staining (Figure. S9A and B). In good agreement with the results of micro-CT, defects covered by PMBA (G/10A/10HM) formed apparent woven bone on week 4, which was then reconstructed into regular lamellar bone on week 8. The G and G/10HM group showed relatively less osteogenesis. Notably, fibrous tissue rather than new bone formation was observed in blank group after healing for 4 or 8 weeks. Similarly, Masson's trichrome staining also revealed more new bone formation in the PMBA group. We can clearly see that our PMBA promoted the formation of well-organized mature lamellar bone (red staining), while only immature woven bone or osteoids (blue staining) were observed in defect treated with G and G/10HM at week 8. The Col-1 immunofluorescence staining also showed consistent results that G/10A/10HM group had more and stronger positive staining areas than other groups (Figure S9C).

To investigate the effect of PMBA on *in vivo* revascularization, we further performed immunohistochemical staining of CD31 (also known as platelet endothelial cell adhesion molecule (PECAM-1) in defect areas at 4 and 8 weeks.[31] Consistent with tube formation assay *in vitro,* all groups exhibited the presence of CD31-positive cells within the defects (Figure. S10A). The neovasculature stained as brown round or oval shapes were mainly concentrated in the surrounding connective tissues, which were part of the newly generated bone tissues. Compared with control groups, the number of blood vessels greatly increased in the defects treated with PMBA, demonstrating its better ability to promote angiogenesis. These promising results indicated that our PMBA could achieve sustained release of L-arginine and Ca^{2+} *in vivo*

to activate NO/cGMP pathway, and finally enhance the formation of new bone and blood vessels. To further validate the role of our PMBA in the activation of NO-cGMP signaling pathway *in vivo*, we performed the immunofluorescence staining of the eNOS and cGMP of the histological sections of rat calvarial defect. In consistent with the *in vitro* analysis, there are much stronger positive eNOS and cGMP staining in the G/10A/10HM group. These results indicated that our PMBA could achieve sustained release of L-arginine and Ca^{2+} *in vivo* to activate the NO/cGMP signalling pathway, and finally enhance the formation of new bone and blood vessel. Taken together, through osteogenic-angiogenic coupling effect, our PMBA could aid/guide stronger and more efficient *in situ* bone regeneration bridging across defects, representing great promise in clinical treatment of fracture patients with compromised bone and vascular regeneration ability.

3. Conclusion

In this study, we have successfully developed a bionic artificial periosteum, PMBA, with similar nanofibrous structure and biological function (support osteogenesis and angiogenesis simultaneously) to natural periosteum. Such nanofibrous hydrogel membranes could be simply fabricated by coordination of electrospinning and subsequent photo-crosslinking of GelMA, Arg-UPEA and nHAMA. The simple but delicate combination of these three biomaterials harmonize superior mechanical and adhesive performances, as well as biocompatibility into PMBA for its use in surgical procedures. The PMBA presented comparable elastic modulus (858.35– 946.86 kPa) to the natural periosteum (0.92–1.93 MPa) and strong tissue adhesion with 165.6 mmHg burst pressure and 520 kPa lap shear strength. Owing to the sustained Ca^{2+} and L-arginine release from nHAMA and Arg-UPEA, respectively, the NO generation in rBMSCs or HUVECs could be subtly orchestrated. The elevated NO level could then activate/upregulate the expression of downstream signaling molecules in the NO-cGMP

pathway, thereby facilitating the retoration of the bone blood supply and reconstruction of the injured periosteum and bone.

Our current work provides a proof-of-concept demonstration of orchestrating the *in vivo* biomaterial progression: that is, the initial material components (i.e., GelMA, Arg-UPEA and nHAMA) endow the scaffold with suitable physical and biological properties, while its degradation products (i.e., Ca^{2+} and L-arginine) are also involved in long-term mediation of physiological activities. This scaffold engineering strategy considers the interactions of organic molecules and inorganic ions during scaffold erosion to enhance tissue repair from the level of biomolecules, cells to tissues. Furthermore, given its cell and growth factor free nature, our PMBA can avoid possible adverse reactions (i.e., ectopic tissue formation and tumor development) and allow for largescale preparation, representing a ready-to-use therapeutic approach for tissue repair. Moreover, our PMBA consists of only naturally derived materials with defined chemical structure and bioactivity, which is much closer towards a safe and efficient scaffold for clinical translation. We believe that our proposed system, in addition to artificial periosteum, can serve directly as a bone adhesive or patch to guide regeneration of various critical-size bone fractures like large skull defects in which the scaffold can bond bone fragments together to achieve adequate *in vivo* fixation and subsequent osteointegration, while withstanding the intracranial pressure changes to prevent brain tissue damage. Altogether, our PMBA with NO/cGMP pathway-coordinated osteogenic-angiogenic coupling effect will aid further development of high-performance bioscaffolds towards tissue engineering of periosteum or bone, and see extensive applications in the clinical field.

Supporting Information
Supporting Information is available from the Wiley Online Library or from the author.

faculty fund (ZVPC) and international capstone project (1. 4Y. XX. 99XD) from The Hong Kong Polytechnic University.

Conflict of Interest
The authors declare no conflict of interest.

References:

[1]   J. Baldwin, F. Wagner, L. Martine, B. Holzapfel, C. Theodoropoulos, O. Bas, F. Savi, C. Werner, E. De-Juan-Pardo, D. Hutmacher, *Biomaterials.* **2017**, 121, 193.

[2]   a) Q. Wang, J. Xu, H. Jin, W. Zheng, X. Zhang, Y. Huang, Z. Qian, *Chin. Chem. Lett.* **2017**, 28, 1801; b) N. Li, J. Song, G. Zhu, X. Li, L. Liu, X. Shi, Y. Wang, *Biomater. Sci.* **2016**, 4, 1554.

[3]   O. D. De Lageneste, A. Julien, R. Abou-Khalil, G. Frangi, C. Carvalho, N. Cagnard, C. Cordier, S. J. Conway, C. Colnot, *Nat. Commun.* **2018**, 9, 1.

[4]   Y. Zhou, F. Chen, S. T. Ho, M. A. Woodruff, T. M. Lim, D. W. Hutmacher, *Biomaterials.* **2007**, 28, 814.

[5]   L. Zhao, J. L. Zhao, L. Wan, S. K. Wang, *Strategies Trauma Limb Reconstr.* **2008**, 3, 57.

[6]   B. Schonmeyr, N. Clavin, T. Avraham, V. Longo, B. J. Mehrara, *Tissue Eng. Part A.* **2009**, 15, 1833.

[7]   T. W. Xin, Y. Gu, R. Y. Cheng, J. C. Tang, Z. Y. Sun, W. Cui, L. Chen, *ACS Appl. Mater. Inter.* **2017**, 9, 41168.

[8]   L. Wu, Y. Gu, L. Liu, J. Tang, J. Mao, K. Xi, Z. Jiang, Y. Zhou, Y. Xu, L. Deng, L. Chen, W. Cui, *Biomaterials.* **2020**, 227, 119555.

[9]   a) X. Sun, Q. Lang, H. Zhang, L. Cheng, Y. Zhang, G. Pan, X. Zhao, H. Yang, Y. Zhang, H. A. Santos, W. Cui, *Adv. Funct. Mater.* **2017**, 27, 1604617; b) X. Zhao, X. Sun, L.

Yildirimer, Q. Lang, Z. Lin, R. Zheng, Y. Zhang, W. Cui, N. Annabi, A. Khademhosseini, *Acta Biomater.* **2017**, 49, 66.

[10]   a) W. Ji, F. Yang, J. Ma, M. J. Bouma, O. C. Boerman, Z. Chen, J. J. van den Beucken, J. A. Jansen, *Biomaterials.* **2013**, 34, 735; b) K. Ren, Y. Wang, T. Sun, W. Yue, H. Zhang, *Mater. Sci. Eng. C* **2017**, 78, 324.

[11]   D. Santos, C. O. Correia, D. M. Silva, P. S. Gomes, M. H. Fernandes, J. D. Santos, V. Sencadas, *Mater. Sci. Eng. C* **2017**, 75, 1184.

[12]   J. S. Fernandes, P. Gentile, M. Martins, N. M. Neves, C. Miller, A. Crawford, R. A. Pires, P. Hatton, R. L. Reis, *Acta Biomater.* **2016**, 44, 168.

[13]   a) A. Assmann, A. Vegh, M. Ghasemi-Rad, S. Bagherifard, G. Cheng, E. S. Sani, G. U. Ruiz-Esparza, I. Noshadi, A. D. Lassaletta, S. Gangadharan, A. Tamayol, A. Khademhosseini, N. Annabi, *Biomaterials* **2017**, 140, 115; b) X. Zhao, Q. Lang, L. Yildirimer, Z. Y. Lin, W. Cui, N. Annabi, K. W. Ng, M. R. Dokmeci, A. M. Ghaemmaghami, A. Khademhosseini, *Adv. Healthc. Mater.* **2016**, 5, 108; c) Z. Yang, Y. Yang, L. Zhang, K. Xiong, X. Li, F. Zhang, J. Wang, X. Zhao, N. Huang, *Biomaterials* **2018**, 178, 1; d) X. Sun, X. Zhao, L. Zhao, Q. Li, M. D'Ortenzio, B. Nguyen, X. Xu, Y. Wen, *J Mater. Chem. B* **2015**, 3, 6368; e) Z. Yuan, X. Zhao, J. Zhao, G. Pan, W. Qiu, X. Wang, Y. Zhu, Q. Zheng, W. Cui, *J Mater. Chem. B* **2015**, 3, 3436.

[14]   a) J. Liu, P. Wang, C. C. Chu, T. Xi, *Colloids Surf. B* **2017**, 159, 78; b) G. Cho, Y. Wu, J. L. Ackerman, *Science.* **2003**, 300, 1123.

[15]   a) J. Liu, P. Wang, C.C. Chu, T. Xi, *Colloids Surf. B* **2017**, 159, 78; b) M. He, L. Sun, X. Fu, S. P. McDonough, C. C. Chu, *Acta Biomater.* **2019**, 84, 114.

[16]   Q. Tu, X. Shen, Y. Liu, Q. Zhang, X. Zhao, M. F. Maitz, T. Liu, H. Qiu, J. Wang, N. Huang, Z. Yang, *Mater. Chem. Front.* **2019**, 3, 265.

[17]   a) W. Zhai, H. Lu, L. Chen, X. Lin, Y. Huang, K. Dai, K. Naoki, G. Chen, J. Chang, *Acta Biomater.* **2012**, 8, 341; b) P. Reher, M. Harris, M. Whiteman, H. K. Hai, S. Meghji, *Bone* **2002**, 31, 236.

[18]   J. Wu, X. Zhao, D. Wu, C. C. Chu, *J Mater. Chem. B* **2014**, 2, 6660.

[19]   X. Xu, Q. Yang, Y. Wang, H. Yu, X. Chen, X. Jing, *Eur. Polym. J.* **2006**, 42, 2081.

[20]   M. Sokolowski, C. Bartsch, V. J. Spiering, S. Prévost, M.S. Appavou, R. Schweins, M. Gradzielski, *Macromolecules.* **2018**, 51, 6936.

[21]   J. Hu, Y. Chen, Y. Li, Z. Zhou, Y. Cheng, *Biomaterials.* **2017**, 112, 133.

[22]   M. He, C. Chu, *Polymer.* **2013**, 54, 4112.

[23]   M. Mehdizadeh, H. Weng, D. Gyawali, L. Tang, J. Yang, *Biomaterials.* **2012**, 33, 7972.

[24]   a) C. P. Weiner, I. Lizasoain, S. A. Baylis, R. G. Knowles, I. G. Charles, S. Moncada, *Proc. Natl. Acad. Sci. U.S.A.* **1994**, 91, 5212; b) S. Moncada, A. Higgs, *N. Engl. J. Med.* **1993**, 329, 2002; c) D. Jagnandan, W. C. Sessa, D. Fulton, *Am. J. Physiol., Cell Physiol.* **2005**, 289, C1024.

[25]   a) G. Cheng, Y. Zhai, K. Chen, J. Zhou, G. Han, R. Zhu, L. Ming, P. Song, J. Wang, *Nitric Oxide.* **2011**, 25, 316; b) C. Coletta, A. Papapetropoulos, K. Erdelyi, G. Olah, K. Modis, P. Panopoulos, A. Asimakopoulou, D. Gero, I. Sharina, E. Martin, C. Szabo, *Proc. Natl. Acad. Sci. U.S.A.* **2012**, 109, 9161.

[26]   E. Wrobel, J. Leszczynska, E. Brzoska, *Cell. Mol. Biol. Lett.* **2016**, 21, 26.

[27]   S. Liu, Y. Zhou, D. Tang, N. Zhou, W. Zheng, Z. Tang, C. Duan, L. Zheng, J. Chen, *Biochem. Biophys. Res. Commun.* **2019**, 519, 1.

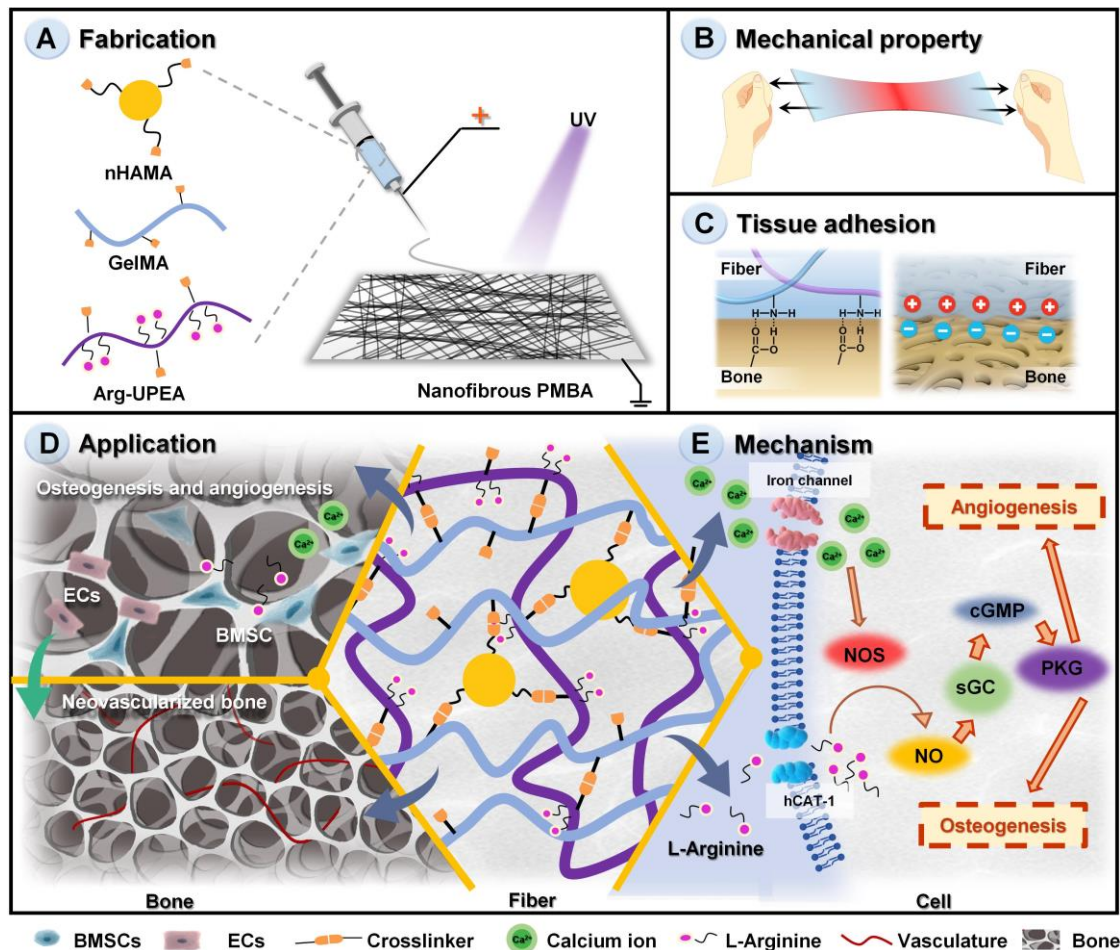[28]   H. Cui, Y. Yu, X. Li, Z. Sun, J. Ruan, Z. Wu, J. Qian, J. Yin, *J Mater. Chem. B* **2019**, 7, 7207.

Figure 1. Schematic illustration of the fabrication, characteristics, mechanism and application of periosteum mimicking bone aid (PMBA). (A) PMBA is fabricated by electrospinning photo-crosslinkable methacrylated gelatin (GelMA), L-arginine-based unsaturated poly (ester amide) (Arg-UPEA) and methacrylated hydroxyapatite nanoparticles (nHAMA). (B) Upon light exposure, these three components crosslink with each other to form an organic-inorganic double network, enhancing the PMBA mechanical properties. (C) Due to the electrostatic attractions and the covalent binding with carboxyl groups of bone tissue surface, this PMBA will also demonstrate superior adhesion performance. After implantation, the PMBA sustainably releases calcium ions and L-arginine to (E) activate/upregulate the NO-cGMP signaling pathway of both BMSCs and ECs, (D) achieving a well-coordinated osteogenic-angiogenic coupling effect and ultimately resulting in accelerated bone regeneration.
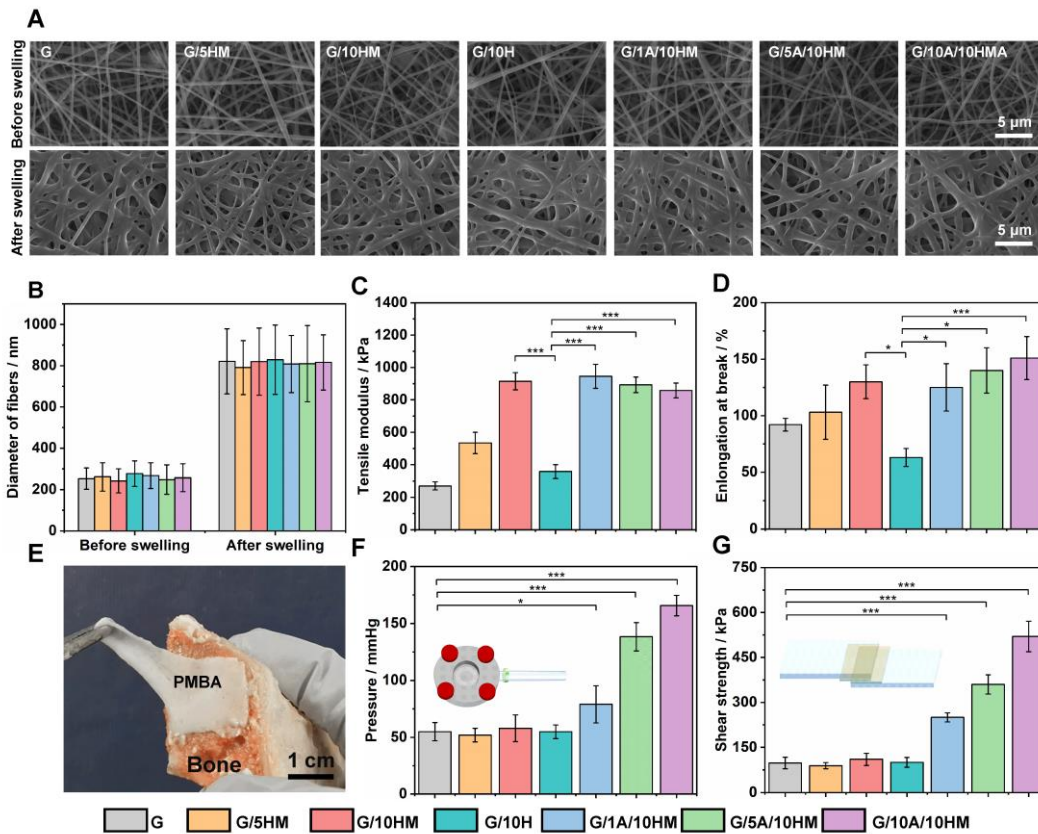
Figure 2. Morphology, mechanical and adhesion strength of PMBA with different contents of nHAMA and Arg-UPEA. (A) Representative SEM images and (B) fiber diameter distribution of different electrospun membranes before and after water sorption. (C) Tensile modulus and (D) elongation at break of prepared electrospun membranes measured by stress-strain curve of tensile compressive test. (E) Photographs of *ex vivo* adhesion of PMBA (G/10HM-10A) to natural porcine bone. Quantification of (F) burst pressure and (G) shear strength of different PMBA. Inserted images showed the representative setup for burst pressure and lap shear measurements, respectively. G, G/5HM, G/10HM, G/10H, G/1A/10HM, G/5A/10HM and G/10A/10HM refer to pristine GelMA, GelMA with 5% nHAMA, GelMA with 10% nHAMA, GelMA with 10% nHA, GelMA with 1% Arg-UPEA and 10% nHAMA, GelMA with 5% Arg-UPEA and 10% nHAMA and GelMA with 10% Arg-UPEA and 10% nHAMA, respectively. Data were presented as mean ± SD and analyzed by one-way ANOVA ($n = 4$ for each sample, $*p < 0.05$, $**p < 0.01$, $***p < 0.001$).
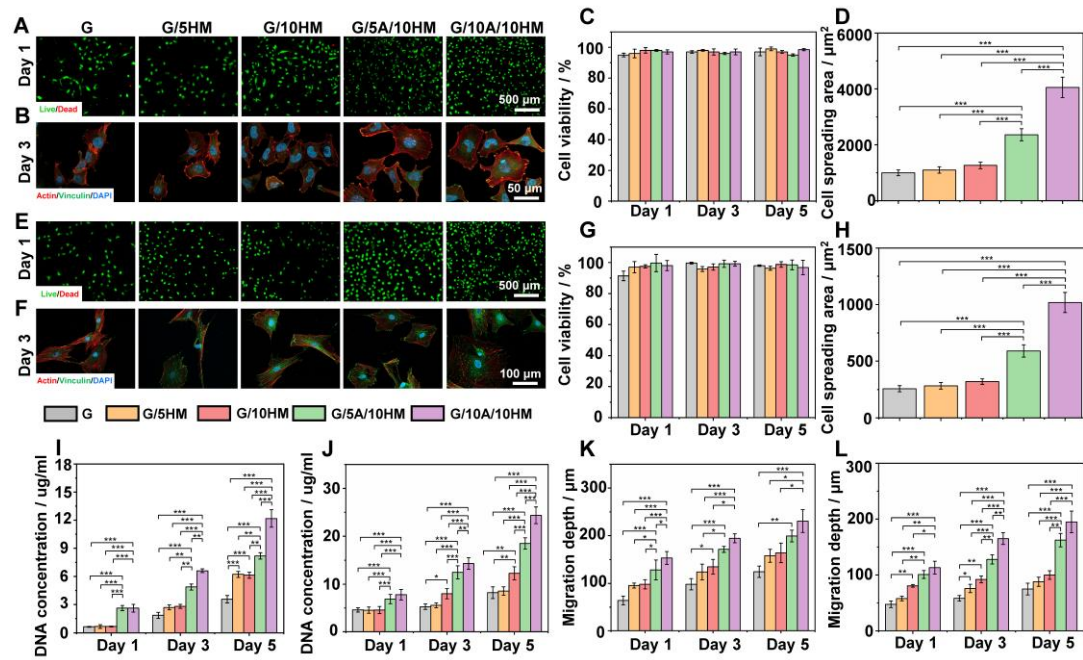
Figure 3. Biocompatibility evaluation of PMBA with different content of nHAMA and Arg-UPEA. Representative Live/Dead images of (A) rBMSCs and (E) HUVECs on different electrospun membranes at day 1. Green fluorescence represents viable cells, while red fluorescence represents dead cells. Representative Actin/DAPI images of (B) rBMSCs and (F) HUVECs on different electrospun membranes at day 3. Green fluorescence indicates cell filaments and blue fluorescence indicates cell nuclei. Quantitative analysis of cell viability of (C) rBMSCs and (G) HUVECs based on Live/Dead staining. Quantification of cell spreading area of (D) rBMSCs and (H) HUVECs based on Actin/DAPI staining. Cell proliferation of (I) rBMSCs and (H) HUVECs on different material surface measured using the Picogreen® DNA assay. Quantification of cell migration depth of (K) rBMSCs and (L) HUVECs into different electrospun membranes with time. G, G/5HM, G/10HM, G/5A/10HM, and G/10A/10HM refer to pristine GelMA, GelMA with 5% nHAMA, GelMA with 10% nHAMA, GelMA with 5% Arg-UPEA and 10% nHAMA, and GelMA with 10% Arg-UPEA and 10% nHAMA, respectively. Data were presented as mean ± SD and analyzed using one-way ANOVA ($n = 4$ for each sample, $*p < 0.05$, $**p < 0.01$, $***p < 0.001$).
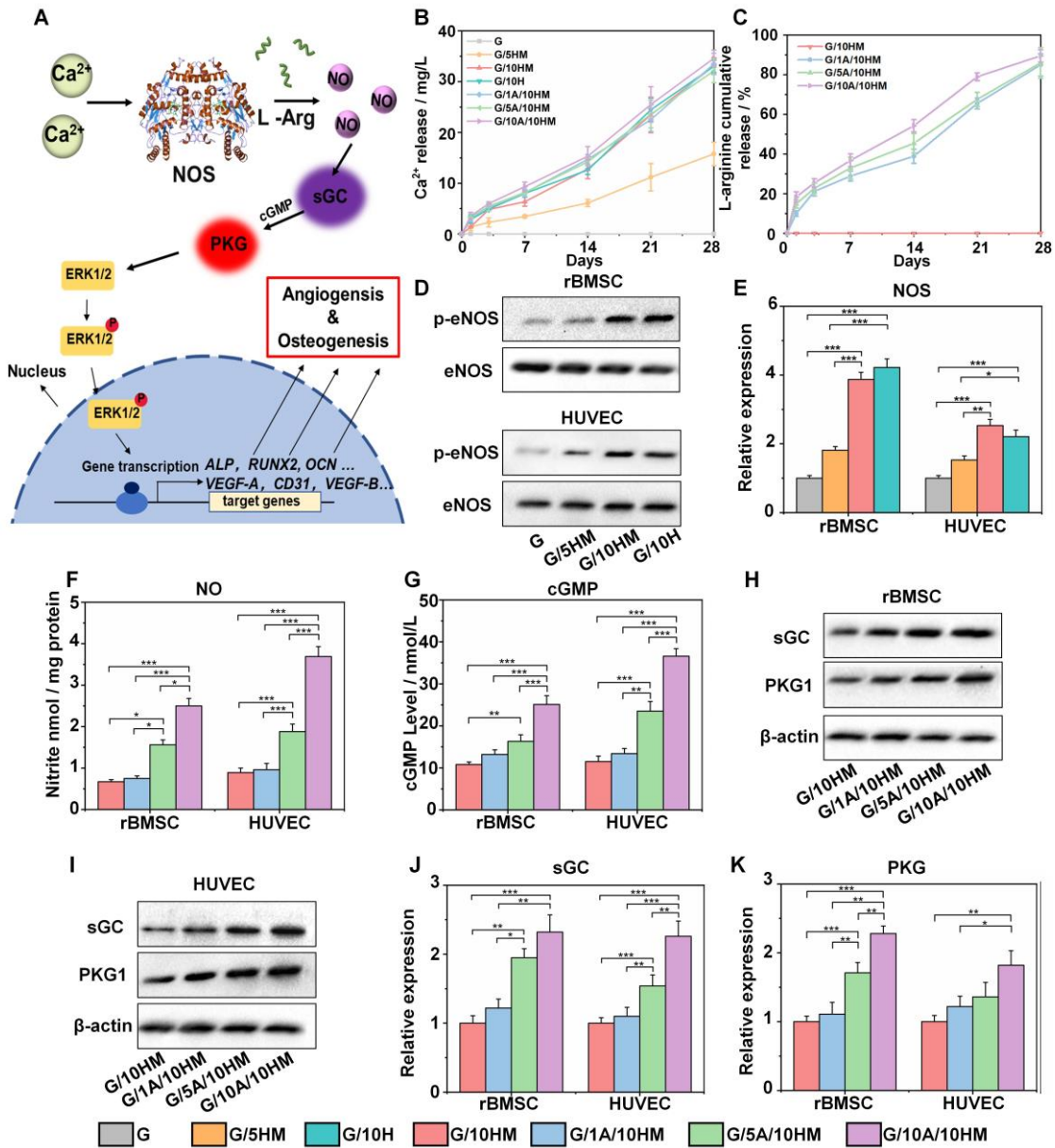
Figure 4. Effect of PMBA on activation of NO/cGMP signaling pathway. (A) Schematic showing the released Ca^{2+} and L-arginine synergistically activate the NO/cGMP pathway, ultimately promoting both osteogenesis and angiogenesis. Release profiles of (B) Ca^{2+} and (C) L-arginine from PMBA with different contents of nHAMA (or nHA) and Arg-UPEA. (D) Representative Western blot and (E) relative optical densitometric quantification showing the protein expressions of p-eNOS and eNOS in rBMSCs or HUVECs. (F) NO generation in rBMSCs or HUVECs indicated by nitrite levels. (G) cGMP expression in rBMSCs or HUVECs on different PMBA. Representative Western blots showing the protein expressions of sCG and PKG1 in (H) rBMSCs or (I) HUVECs. The corresponding quantitative analysis was performed to confirm the protein changes of (J) sCG and (K) PKG1. G, G/5HM, G/10H, G/10HM, G/1A/10HM, G/5A/10HM and G/10A/10HM refer to pristine GelMA, GelMA with 5% nHAMA, GelMA with 10% nHA, GelMA with 10% nHAMA, GelMA with 1% Arg-UPEA and 10% nHAMA, GelMA with 5% Arg-UPEA and 10% nHAMA and GelMA with 10% Arg-UPEA and 10% nHAMA, respectively. Data were presented as mean $\pm$ SD and analyzed by one-way ANOVA ($n = 3$ for each sample, $*p < 0.05$, $**p < 0.01$, $***p < 0.001$).
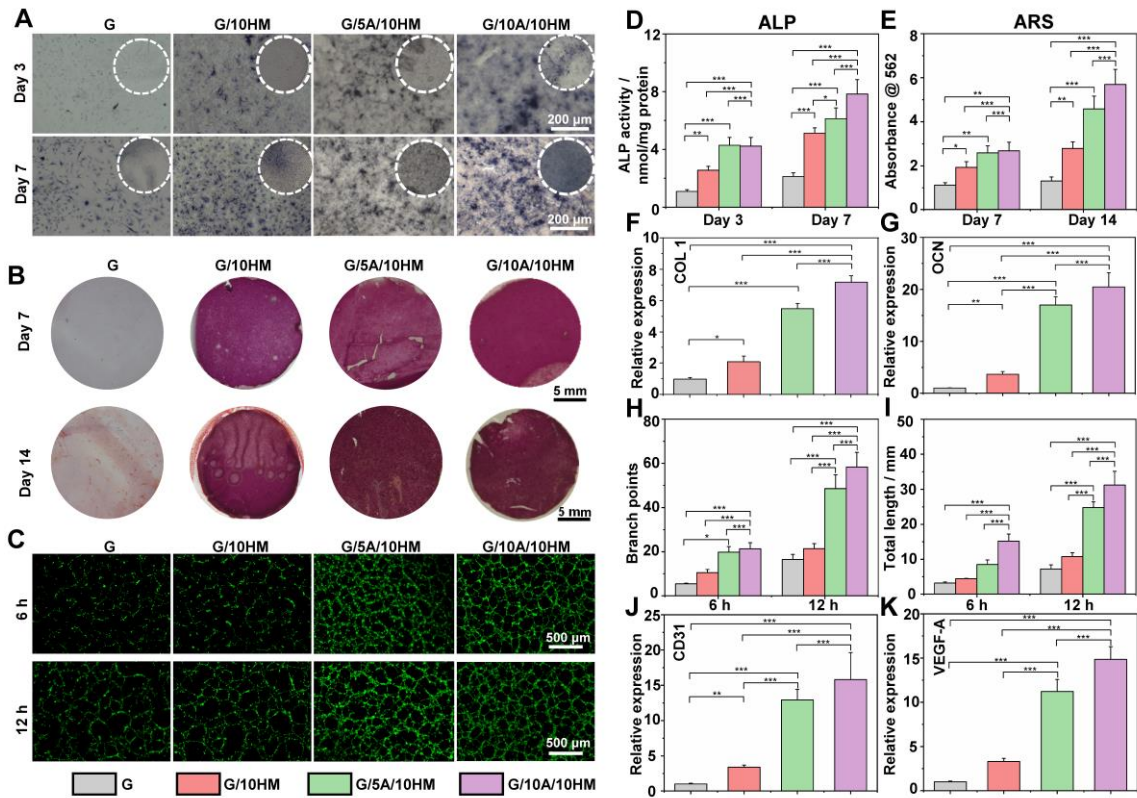
Figure 5. *In vitro* osteogenesis and angiogenesis potential of PMBA with different contents of nHAMA and Arg-UPEA. (A) Representative ALP staining images and (D) quantitative analysis of ALP activity of rBMSCs on day 3 and 7. (B) Representative ARS images and (E) quantitative analysis of calcium deposition of rBMSCs on day 7 and 14. qRT-PCR analysis of osteogenesis-related gene expressions including (F) COL-1 and (G) OCN. (C) Representative fluorescence images showing the endothelial network formation in HUVECs after co-culture for 6 and 12 h. Quantification of (H) branch points and (I) total length in HUVECs. qRT-PCR analysis of angiogenesis-related gene expressions including (J) CD31 and (K) VEGF. G, G/10HM, G/5A/10HM, and G/10A/10HM refer to pristine GelMA, GelMA with 10% nHAMA, GelMA with 5% Arg-UPEA and 10% nHAMA, and GelMA with 10% Arg-UPEA and 10% nHAMA, respectively. Data were presented as mean ± SD and analyzed by one-way ANOVA ($n = 4$ for each sample, $*p < 0.05$, $**p < 0.01$, $***p < 0.001$).
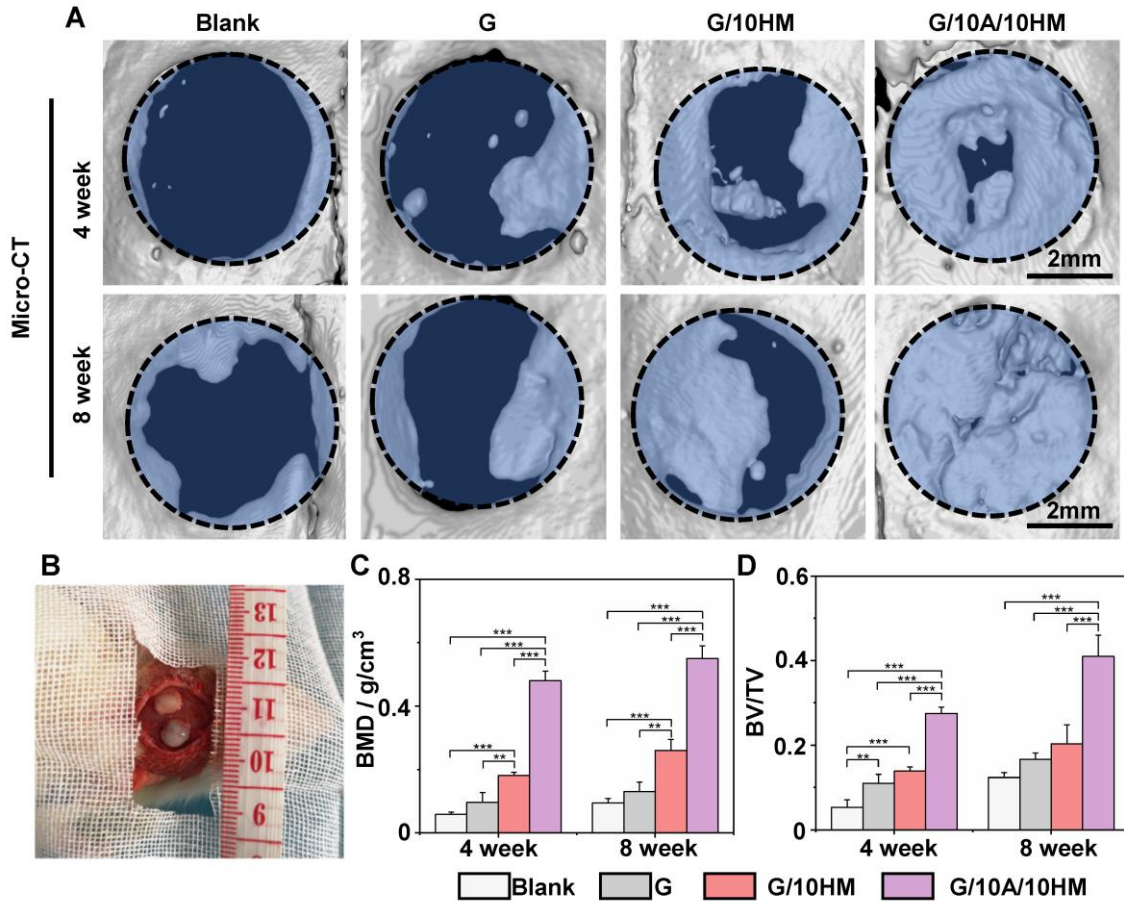
21

Figure 6. *In vivo* bone regeneration therapeutic efficacy of PMBA. (A) 3D reconstructed micro-CT images of defect areas showing the influences of different scaffolds on the new bone formation after implantation for 4 and 8 weeks. (B) A representative photograph showing two bilateral bone and periosteal defects were created on the rat skull. Quantitative statistic of (C) BMD and (C) BV/TV of the newly formed bone at week 4 and 8. BMD: bone mineral density; BV/TV: bone volume/total volume. G, G/10HM, and G/10A/10HM refer to pristine GelMA, GelMA with 10% nHAMA, and GelMA with 10% Arg-UPEA and 10% nHAMA, respectively. Data were presented as mean ± SD and analyzed by one-way ANOVA ($n = 6$ for each sample, *$p < 0.05$, **$p < 0.01$, ***$p < 0.001$)

A periosteum mimicking bone aid (PMBA) with superior mechanical and bioactive properties is developed. The methacrylated gelatin (GelMA) and L-arginine-based unsaturated poly (ester amide) (Arg-UPEA) equip PMBA with superior adhesion properties, while the methacrylated hydroxyapatite nanoparticles (nHAMA) significantly increase its mechanical performances. Calcium ions and L-arginine released can coordinate to co-activate NO-cGMP signaling pathway and achieve osteogenic-angiogenic coupling effect.

Yuhe Yang, Tianpeng Xu, Qiang Zhang, Yun Piao, Ho Pan Bei, Xin Zhao*

Biomimetic, stiff and adhesive periosteum with osteogenic-angiogenic coupling effect for bone regeneration
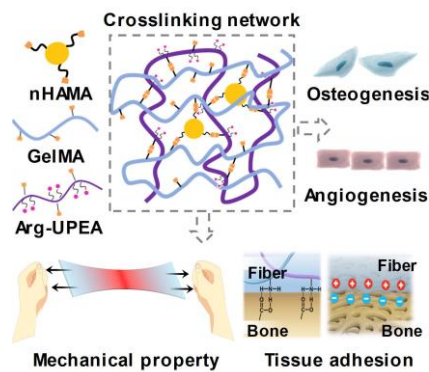
Reference:

[1]   J. Baldwin, F. Wagner, L. Martine, B. Holzapfel, C. Theodoropoulos, O. Bas, F. Savi, C. Werner, E. De-Juan-Pardo, D. Hutmacher, *Biomaterials* **2017**, 121, 193.

[2]   a) Q. Wang, J. Xu, H. Jin, W. Zheng, X. Zhang, Y. Huang, Z. Qian, *Chinese Chemical Letters* **2017**, 28, 1801; b) X. Zhao, S. Liu, L. Yildirimer, H. Zhao, R. Ding, H. Wang, W. Cui, D. Weitz, *Advanced Functional Materials* **2016**, 26, 2809.

[3]   O. D. De Lageneste, A. Julien, R. Abou-Khalil, G. Frangi, C. Carvalho, N. Cagnard, C. Cordier, S. J. Conway, C. Colnot, *Nature communications* **2018**, 9, 1.

[4]   Y. Zhou, F. Chen, S. T. Ho, M. A. Woodruff, T. M. Lim, D. W. Hutmacher, *Biomaterials* **2007**, 28, 814.

[5]   L. Zhao, J. L. Zhao, L. Wan, S. K. Wang, *Strategies Trauma Limb Reconstr* **2008**, 3, 57.

[6]   B. Schonmeyr, N. Clavin, T. Avraham, V. Longo, B. J. Mehrara, *Tissue Engineering Part A* **2009**, 15, 1833.

[7]   T. W. Xin, Y. Gu, R. Y. Cheng, J. C. Tang, Z. Y. Sun, W. Cui, L. Chen, *Acs Applied Materials & Interfaces* **2017**, 9, 41168.

[8]   L. Wu, Y. Gu, L. Liu, J. Tang, J. Mao, K. Xi, Z. Jiang, Y. Zhou, Y. Xu, L. Deng, L. Chen, W. Cui, *Biomaterials* **2020**, 227, 119555.

[9]   X. Zhao, X. Sun, L. Yildirimer, Q. Lang, Z. Y. W. Lin, R. Zheng, Y. Zhang, W. Cui, N. Annabi, A. Khademhosseini, *Acta Biomater* **2017**, 49, 66.

[10]   a) W. Ji, F. Yang, J. Ma, M. J. Bouma, O. C. Boerman, Z. Chen, J. J. van den Beucken, J. A. Jansen, *Biomaterials* **2013**, 34, 735; b) K. Ren, Y. Wang, T. Sun, W. Yue, H. Zhang, *Mater Sci Eng C Mater Biol Appl* **2017**, 78, 324.

[11]   D. Santos, C. O. Correia, D. M. Silva, P. S. Gomes, M. H. Fernandes, J. D. Santos, V. Sencadas, *Materials Science & Engineering C-Materials for Biological Applications* **2017**, 75, 1184.

[12]   J. S. Fernandes, P. Gentile, M. Martins, N. M. Neves, C. Miller, A. Crawford, R. A. Pires, P. Hatton, R. L. Reis, *Acta Biomater* **2016**, 44, 168.

[13]   a) A. Assmann, A. Vegh, M. Ghasemi-Rad, S. Bagherifard, G. Cheng, E. S. Sani, G. U. Ruiz-Esparza, I. Noshadi, A. D. Lassaletta, S. Gangadharan, A. Tamayol, A. Khademhosseini, N. Annabi, *Biomaterials* **2017**, 140, 115; b) X. Zhao, Q. Lang, L. Yildirimer, Z. Y. Lin, W. Cui, N. Annabi, K. W. Ng, M. R. Dokmeci, A. M. Ghaemmaghami, A. Khademhosseini, *Adv Healthc Mater* **2016**, 5, 108; c) Z. Yang, Y. Yang, L. Zhang, K. Xiong, X. Li, F. Zhang, J. Wang, X. Zhao, N. Huang, *Biomaterials* **2018**, 178, 1; d) X. Sun, X. Zhao, L. Zhao, Q. Li, M. D'Ortenzio, B. Nguyen, X. Xu, Y. Wen, *J Mater Chem B* **2015**, 3, 6368; e) Z. Yuan, X. Zhao, J. Zhao, G. Pan, W. Qiu, X. Wang, Y. Zhu, Q. Zheng, W. Cui, *J Mater Chem B* **2015**, 3, 3436.

[14]   a) J. Liu, P. Wang, C. C. Chu, T. Xi, *Colloids Surf B Biointerfaces* **2017**, 159, 78; b) G. Cho, Y. Wu, J. L. Ackerman, *Science* **2003**, 300, 1123.

[15]   M. He, L. Sun, X. Fu, S. P. McDonough, C. C. Chu, *Acta Biomater* **2019**, 84, 114.

[16]   Q. Tu, X. Shen, Y. Liu, Q. Zhang, X. Zhao, M. F. Maitz, T. Liu, H. Qiu, J. Wang, N. Huang, Z. Yang, *Materials Chemistry Frontiers* **2019**, 3, 265.

[17]   a) W. Zhai, H. Lu, L. Chen, X. Lin, Y. Huang, K. Dai, K. Naoki, G. Chen, J. Chang, *Acta Biomater* **2012**, 8, 341; b) P. Reher, M. Harris, M. Whiteman, H. K. Hai, S. Meghji, *Bone* **2002**, 31, 236.

[18]   J. Wu, X. Zhao, D. Wu, C. C. Chu, *J Mater Chem B* **2014**, 2, 6660.

[19]   X. Xu, Q. Yang, Y. Wang, H. Yu, X. Chen, X. J. E. p. j. Jing, **2006**, 42, 2081.

[20]   M. Sokolowski, C. Bartsch, V. J. Spiering, S. Prévost, M.-S. Appavou, R. Schweins, M. Gradzielski, *J Macromolecules* **2018**, 51, 6936.

[21] M. Gong, C. Chi, J. Ye, M. Liao, W. Xie, C. Wu, R. Shi, L. Zhang, *Colloids and Surfaces B: Biointerfaces* **2018**, 170, 201.

[22] J. Hu, Y. Chen, Y. Li, Z. Zhou, Y. Cheng, *Biomaterials* **2017**, 112, 133.

[23] M. He, C.-C. Chu, *Polymer* **2013**, 54, 4112.

[24] a) S. H. McBride, S. F. Evans, M. L. K. Tate, *Journal of biomechanics* **2011**, 44, 1954; b) J. Bertram, Y. Polevoy, D. Cullinane, *Bone* **1998**, 22, 669.

[25] M. Mehdizadeh, H. Weng, D. Gyawali, L. Tang, J. Yang, *Biomaterials* **2012**, 33, 7972.

[26] a) C. P. Weiner, I. Lizasoain, S. A. Baylis, R. G. Knowles, I. G. Charles, S. Moncada, *Proc Natl Acad Sci U S A* **1994**, 91, 5212; b) S. Moncada, A. Higgs, *New England Journal of Medicine* **1993**, 329, 2002; c) D. Jagnandan, W. C. Sessa, D. Fulton, *Am J Physiol Cell Physiol* **2005**, 289, C1024.

[27] a) G. Cheng, Y. Zhai, K. Chen, J. Zhou, G. Han, R. Zhu, L. Ming, P. Song, J. Wang, *Nitric Oxide* **2011**, 25, 316; b) C. Coletta, A. Papapetropoulos, K. Erdelyi, G. Olah, K. Modis, P. Panopoulos, A. Asimakopoulou, D. Gero, I. Sharina, E. Martin, C. Szabo, *Proc Natl Acad Sci U S A* **2012**, 109, 9161.

[28] E. Wrobel, J. Leszczynska, E. Brzoska, *J Cellular molecular biology letters* **2016**, 21, 26.

[29] S.-L. Liu, Y.-M. Zhou, D.-B. Tang, N. Zhou, W.-W. Zheng, Z.-H. Tang, C.-W. Duan, L. Zheng, J. Chen, *J Biochemical biophysical research communications* **2019**, 519, 1.

[30] P. P. Spicer, J. D. Kretlow, S. Young, J. A. Jansen, F. K. Kasper, A. G. Mikos, *Nature protocols* **2012**, 7, 1918.

[31] H. Cui, Y. Yu, X. Li, Z. Sun, J. Ruan, Z. Wu, J. Qian, J. Yin, *J Journal of Materials Chemistry B* **2019**, 7, 7207.